Nanoscale

ROYAL SOCIETY OF CHEMISTRY

PAPER

View Article Online
View Journal | View Issue

Cite this: *Nanoscale*, 2020, **12**, 16489

Large-area periodic arrays of gold nanostars derived from HEPES-, DMF-, and ascorbic-acid-driven syntheses†

Trevor B. Demille,[a] Robert A. Hughes,[a] Nathaniel Dominique,[b] Jacob E. Olson,[b] Sergei Rouvimov,[c] Jon P. Camden[b] and Svetlana Neretina *[a,b]

With arms radiating from a central core, gold nanostars represent a unique and fascinating class of nanomaterials from which extraordinary plasmonic properties are derived. Despite their relevance to sensing applications, methods for fabricating homogeneous populations of nanostars on large-area planar surfaces in truly periodic arrays is lacking. Herein, the fabrication of nanostar arrays is demonstrated through the formation of hexagonal patterns of near-hemispherical gold seeds and their subsequent exposure to a liquid-state chemical environment that is conducive to colloidal nanostar formation. Three different colloidal nanostar protocols were targeted where HEPES, DMF, and ascorbic acid represent a key reagent in their respective redox chemistries. Only the DMF-driven synthesis proved readily adaptable to the substrate-based platform but nanostar-like structures emerged from the other protocols when synthetic controls such as reaction kinetics, the addition of Ag^+ ions, and pH adjustments were applied. Because the nanostars were derived from near-hemispherical seeds, they acquired a unique geometry that resembles a conventional nanostar that has been truncated near its midsection. Simulations of plasmonic properties of this geometry reveal that such structures can exhibit maximum near-field intensities that are as much as seven-times greater than the standard nanostar geometry, a finding that is corroborated by surface-enhanced Raman scattering (SERS) measurements showing large enhancement factors. The study adds nanostars to the library of nanostructure geometries that are amenable to large-area periodic arrays and provides a potential pathway for the nanofabrication of SERS substrates with even greater enhancements.

Received 29th May 2020,
Accepted 23rd July 2020

DOI: 10.1039/d0nr04141f

rsc.li/nanoscale

1. Introduction

Plasmonic nanostructures characterized by highly branched spiked morphologies are valued for the intense electromagnetic near-fields that form near their sharp tips,[1] the generation of high concentrations of hot electrons,[2] and a highly tunable localized surface plasmon resonance (LSPR).[3] Such structures, which are broadly termed as nanostars, exhibit a wide range of morphologies that encompass those with symmetric arms radiating from a central core[4–7] as well as highly erratic branched configurations.[8–10] The spikes can be long and protruding[9] or short and pointed[10] and where the overall size can be highly variable. Collectively, these structures have demonstrated an exceedingly high degree of utility. Chemical and biological sensing applications, for example, have effectively utilized a wide range of modalities including surface-enhanced Raman scattering (SERS),[11–20] refractive index sensing,[21,22] metal-enhanced fluorescence,[23] chemiluminescence,[24] and two-photon photoluminescence.[25] Additionally, photothermal properties have been used in theranostics[26–33] and photochemical properties have been exploited in important photocatalytic reactions such as water splitting.[2,34] The unique geometry of nanostars has also led to their use in the fabrication of probes for scanning probe microscopies based on tip-enhanced Raman scattering (TERS) and tip-enhanced fluorescence (TEF).[35] Of specific relevance to this work is that many of these applications require that nanostars be immobilized on a supporting substrate.

The colloidal synthesis of Au nanostars requires growth pathways that override the thermodynamic tendency that this isotropic metal has to form highly symmetric faceted struc-

[a]*College of Engineering, University of Notre Dame, Notre Dame, Indiana 46556, USA. E-mail: sneretina@nd.edu*
[b]*Department of Chemistry & Biochemistry, University of Notre Dame, Notre Dame, Indiana 46556, USA*
[c]*Notre Dame Integrated Imaging Facility, University of Notre Dame, Notre Dame, Indiana 46556, USA*

†Electronic supplementary information (ESI) available. See DOI: 10.1039/d0nr04141f

tures while at the same time relying on the local activation and emergence of branched structures along specific crystallographic directions. To do so requires the formation of nucleation points from which accelerated highly directional growth occurs. Numerous pathways have now emerged to achieve this outcome where twin defects,[7] Ag^+ ions,[4] capping agents,[10] growth kinetics,[25] and combinations thereof are used to induce branched morphologies. In broad terms, these growth modes can be categorized as seeded and unseeded, where the latter typically provides for ease of synthesis at the expense of polydispersity.[3] With numerous seed-mediated protocols for nanostar syntheses now discovered and thoroughly investigated, it has become apparent that, despite their seemingly erratic nature, this class of nanostructures is amenable to synthetic controls that are able to dictate size,[22] shape,[4] the number of arms,[22] and the arm-to-core size ratio.[2]

With many applications requiring the placement of plasmonic nanostars on surfaces, proof-of-principle demonstrations have often relied on the dispersal of colloids onto substrates by drop-casting or through their electrostatic attachment to functionalized surfaces.[15,18,36] Applications requiring that the plasmonic nanostructures be placed on a conducting surface have resorted to the electrochemical deposition of nanostars onto ITO-coated substrates.[37] Although these methods have proven viable, they are unable to assert control over nanostructure placement. Methods to achieve organized configurations of nanostars have used either e-beam lithography to define two-dimensional nanostars over small areas[38] or block-copolymer micelle nanolithography to obtain larger areas but where long-range order is lacking.[39] Methods to fabricate truly periodic arrays of near-identical nanostars over large areas has not yet been demonstrated.

Numerous nanofabrication strategies have been employed that combine conventional lithographic techniques with well-established nanomaterial synthesis routes to yield periodic arrays of architecturally complex nanostructures.[40,41] Such techniques, however, have not previously proven successful in the fabrication of nanostar arrays. Herein, we apply three different seed-mediated nanostar syntheses routes to periodic arrays of substrate-immobilized Au seeds formed using a combination of nanoimprint lithography and templated-assembly. For each case, it is shown that nanostars form with a fundamentally different character than those obtained using the analogous colloidal synthesis due to an apparent truncation of the nanostar by the substrate. Simulations of the plasmonic response reveal that this unique nanostar geometry leads to a truncation-induced red shift and strong near fields near the nanostar–substrate interface, a property that is of high relevance to SERS applications.

2. Results

2.1. Synthetic scheme for substrate-immobilized Au nanostars

With the goal of forming substrate-immobilized nanostars, a synthetic scheme was devised in which substrate-bound Au seeds are first prepared using a vapor-phase directed-assembly process and then exposed to a liquid-phase synthesis known to promote the formation of branched morphologies with sharp tips. The expectation was that nanostars would evolve from the substrate-immobilized seeds as well as from spontaneously nucleated seeds that give rise to a colloidal component. The substrate-based Au seeds used in this study were prepared in periodic arrays using procedures[42] and techniques[43] described elsewhere. The arrayed format offers an excellent platform for such studies since it allows for spontaneous nucleation events on the substrate surface to be readily distinguished from those that are seed-mediated. The seeds, shown in Fig. 1a, are near-hemispherical structures with a diameter of approximately 65 nm and are predominantly oriented with their [111]-axis normal to the substrate surface.[42] Although it is recognized that these seeds are significantly larger than those commonly used in seed-mediated nanostar growth modes, the fact that they are well-bonded to the substrate and exhibit a strong propensity for the formation of twin defects,[42] a defect associated with the formation of nanostar limbs,[44] makes them an unknown, yet intriguing, nucleation site for substrate-based nanostar growth modes. Three well-established nanostar colloidal growth modes were targeted,[19,25,36] where each is known to yield a unique morphology. For the purpose of this study, they are termed as HEPES-, DMF-, and AA-driven nanostar syntheses after a key reagent used in their redox chemistry. Each of these syntheses, as well as the anticipated colloidal nanostar architecture, is shown schematically in Fig. 1b–d. For each case, key synthetic levers were varied so as to optimize and gain control over nanostar formation on the substrate surface.

2.2. Nanostar synthesis modes

2.2.1. HEPES-driven growth of substrate-immobilized Au nanostars. HEPES is a water-soluble Good's buffer that is commonly used in biological applications.[36] Its effectiveness as a both a reducing and shape-directing agent in the synthesis of Au nanostars was first demonstrated in an aqueous room-temperature protocol forwarded by Xie *et al.*[36] that requires only HEPES, $HAuCl_4$, and NaOH as reagents. The protocol, which has since been extended to other Good's buffers,[45] is able to exert control over the nanostar architecture through parametric controls offered by the HEPES/$HAuCl_4$ ratio,[45,46] pH,[21,45] and the degree to which the reagents are stirred.[45] HEPES-driven colloidal nanostar syntheses have utilized both seedless[36,45–50] and seed-mediated[15,21] modalities and have incorporated Ag^+ ions as a shape-directing agent.[49] Initial efforts to enact the HEPES-driven growth mode on substrate-immobilized seeds following the Xie protocol proved unsatisfactory. Even though colloidal structures generated from spontaneously generated seeds gave rise to nanostars, the reduction of Au^{3+} onto the substrate-bound seeds did not lead to the formation of limbs but instead resulted in a somewhat roughened surface morphology.

With standard colloidal growth conditions proving unsuitable, the parameter space of the synthesis was explored with the

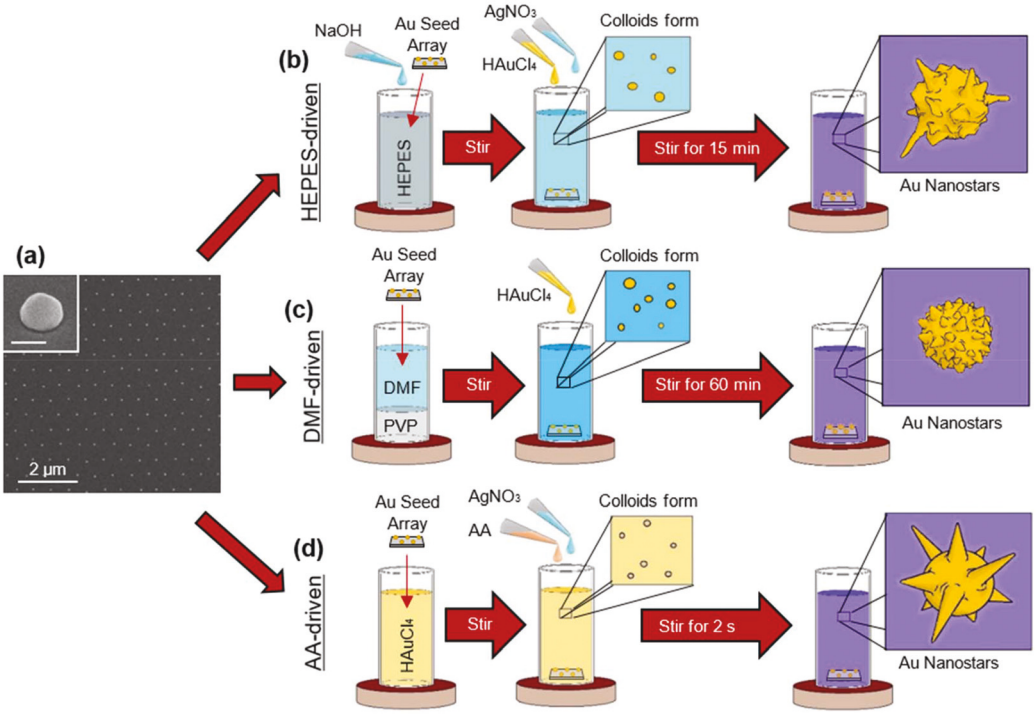

Fig. 1 (a) SEM of a periodic array of substrate-supported Au seeds (inset scale bar is 50 nm). Schematic representation of the (b) HEPES-, (c) DMF-, and (d) AA-driven nanostar growth modes into which seed arrays are placed. A schematic of nanostar geometry that is expected to emerge as a colloid is shown to the right of each growth mode.

goal of defining the reaction conditions needed to realize branched morphologies. It was determined that increases to the HEPES/$HAuCl_4$ ratio in combination with the addition of small quantities of Ag^+ ions to the reaction mixture yielded the most favorable results. Increases to the HEPES/$HAuCl_4$ ratio alone led to progressively more nucleation at the seed surface and eventually to the emergence of a rough jagged morphology but where no limbs were formed (see ESI, Fig. S1†). Fig. 2a shows the morphology obtained when this ratio is increased by a factor of six over what is used in the Xie protocol[36] and by similar factors when compared to other HEPES-driven colloidal syntheses.[21,45] Further increases to this ratio proved detrimental in that it saw the emergence of faceted growth where even some small nanocube-like structures were clearly visible. The addition of small quantities of Ag^+ ions, however, led to dramatic morphological changes. Fig. 2b and c shows the morphologies obtained when 80 and 200 μM concentrations of $AgNO_3$ are included as part of the reaction mixture. The lower concentration leads to the formation of a limbless core encircled by a single leaf-like formation that is adjacent to the substrate surface. For the higher concentration, limb formation prevails with each of the arrayed structures showing a high density of protrusions emanating from a central core. Histograms of the Au seed and resulting nanostar diameters (Fig. 2d and e) show that the synthesis resulted in an increase in size from 72 to 236 nm and an estimated 10-fold increase in cross-sectional area. Histograms for the 0 and 80 μM samples are provided as ESI (Fig. S2†). Fig. 2f shows the absorbance spectra for all three arrays where the data has been normalized to allow for easier comparison but where it should be recognized that the 80 and 200 μM samples show a 3- and 4-fold increase in the absorbance maximum when compared to the $AgNO_3$-free synthesis. The spectra for the nanostars is striking in that it has a narrow LSPR peak centered at 960 nm, a feature consistent with the relatively homogeneous size distribution exhibited by the arrayed nanostars.

The alterations to the HEPES-driven synthesis that are needed to promote a seed-mediated substrate-based nanostar growth mode still give rise to the simultaneous formation of a colloidal component. The changes made, however, have a negative impact on the nanostar colloidal growth mode. The increased HEPES/$HAuCl_4$ ratio, which gave rise to the structures shown in Fig. 2a, resulted in colloidal structures with a roundish morphology (Fig. 2g) that exhibited an LSPR centered at 550 nm (see ESI, Fig. S3†). The introduction of Ag^+ ions into the growth mixture, to some extent, remedied the colloidal growth mode in that nanostructures evolved exhibiting erratic plate-like features (Fig. 2h) with a broad LSPR centered at 805 nm but where few similarities exist between the colloid and the substrate-based structures. Together, these results show that spontaneously generated colloidal structures act as a poor indicator for predicting the nanostructures that will evolve on the substrate surface even when identical reaction conditions are used.

2.2.2. DMF-driven growth of substrate-immobilized Au nanostars. DMF has been widely used as both a solvent and

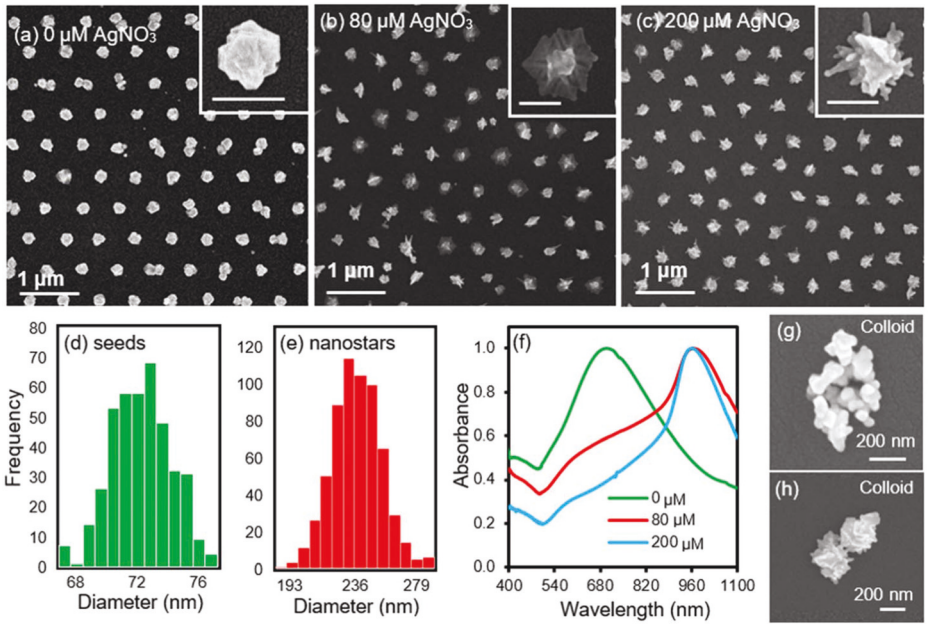

Fig. 2 SEM images of periodic arrays of Au nanostars derived from a HEPES-driven reaction that utilized (a) 0, (b) 80, and (c) 200 μM concentrations of Ag^+ ions (inset scale bar is 200 nm). Histograms of the (d) seed and (e) nanostar (NS) diameters for the 200 μM $AgNO_3$ sample. (f) The absorbance spectra showing the plasmon resonance obtained for each of the arrays. SEM images of the nanostar colloid formed in the (g) absence of Ag^+ ions and (h) when using a 200 μM concentration of Ag^+.

reducing agent in the synthesis of noble metal nanostructures.[51,52] When used in combination with PVP, which by itself is an effective reducing, shape-control, and stabilization agent,[53] DMF-based syntheses give rise to a set of robust colloidal protocols that are able to generate a wide variety of sophisticated nanostructures in high yield.[19,51,54–56] Among these is a seed-mediated room-temperature protocol devised by Kumar *et al.*[19] that gives rise to nanostars when $HAuCl_4$, PVP, and DMF are appropriately combined.[22] This and related syntheses,[7,10,24,57,58] require that PVP be added in high concentrations to (i) act as an effective reducing agent and (ii) form complexes with the DMF solvent that regulate the growth pathway.[10,58] These DMF-driven syntheses have been carried out using both seedless[10,22,57,58] and seed-mediated[7,19,24] modalities where controls are placed on nanostructure properties through variations to the $HAuCl_4$ and PVP concentrations,[19,22] the use of additional reagents such as NaOH,[22,57] HCl,[58] and DMA[7] (dimethylamine), and the introduction of icosahedral seeds.[7]

The adaptation of the DMF-driven growth mode to the use of substrate-truncated seeds proved relatively straightforward. Fig. 3a and b shows tilted- and top-view images of a periodic array of nanostars formed in a DMF solvent using only $HAuCl_4$ and PVP as reagents. The structures exhibit a central core from which short limbs with rather sharp tips emanate, a feature commonly expressed by nanostars derived from DMF-driven colloidal growth modes.[10,22,57] The substrate-truncated nanostars are produced with what is essentially a 100% yield with excellent size uniformity as characterized by the histogram shown in Fig. 3c that displays an average nanostar diameter of 166 nm with a full width at half maximum of 18 nm. This, once again, agrees with DMF-driven colloidal growth modes in that they too show a high degree of size uniformity when using seed-mediated syntheses.[7,19] With pH changes due to the addition of NaOH proving beneficial to colloidal nanostar syntheses, this parameter was systematically varied. NaOH additions maintained a similarly sized core with no measurable changes to the number of limbs but where limb growth was suppressed (see ESI, Fig. S4†). This behavior is reflected in the corresponding absorbance curves (Fig. 3d) that show both increasing blue shifts and successive declines in the LSPR absorbance as the NaOH concentration is increased. Although a similar decline in the LSPR absorbance is observed in colloidal syntheses, the substrate-based results are somewhat contrary in that NaOH was found to increase the number of limbs on the colloidal structures.[22,57] For the substrate-based structures, it is also noted that the relatively large core diameter coupled with relatively short limbs increases the degree of overlap between the nanostar limb and core LSPR modes such that only one broad peak is observed, an effect that is further exacerbated by a substrate-induced broadening of the LSPR peaks.[59] Neither the addition of HCl nor $AgNO_3$ to the NaOH-free synthesis resulted in improvements to the nanostar geometry, with the former giving rise to more plate-like limbs (see ESI, Fig. S5†) and the latter severely limiting the reduction of Au^{3+} onto the seeds (see ESI, Fig. S6†).

As was the case for the HEPES-driven synthesis, substrate-based nanostar formation is accompanied by the formation of colloidal nanostructures. The emergence of the colloidal component, however, occurs on much larger timescales as is made

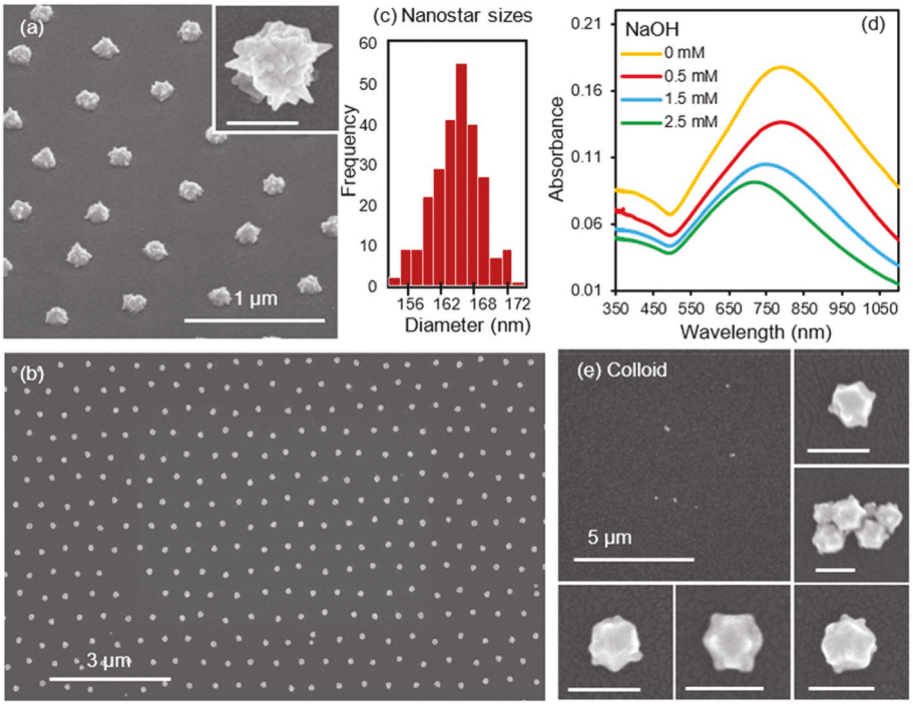

Fig. 3 SEM images of a periodic array of Au nanostars derived from a NaOH-free DMF-driven growth mode from a (a) 50° tilted- and (b) top-view. (c) Histogram of the Au nanostar diameters. (d) Absorbance spectra showing the LSPR for DMF-derived nanostars synthesized using various NaOH concentrations. (e) SEM images of a surface that is sparsely populated with drop-cast colloidal nanostars as well as high magnification images of individual structures. The scale bars for all insets are 150 nm.

evident by the clear to dark purple color change that occurs over a 1 h period. The long durations required for the DMF-driven synthesis is indicative of the relatively slow kinetics associated with this growth pathway.[19,20] Fig. 3e shows SEM images of the colloidal nanostars obtained through centrifugation followed by drop-casting for the NaOH-free synthesis. The structures display the characteristic Au nanostar morphology, although the limbs are considerably more rounded than those formed on the substrate-based structures. It is noted that the addition of $AgNO_3$ to the synthesis caused the growth solution to remain clear even for durations lasting as long as 24 h, a result that is consistent with the seeded surface showing little deposition when subjected to the same growth conditions (see ESI, Fig. S6†).

2.2.3. AA-driven growth of substrate-immobilized Au nanostars. Ascorbic acid, which is a weak reducing agent under non-alkaline conditions, has been widely used in nanostructure synthesis.[52] When quickly added to an aqueous mixture of $HAuCl_4$ and $AgNO_3$, it, within seconds, gives rise to a population of nanostars with long and well-defined limbs. The role of Ag^+ in this reaction is as a shape-directing agent where its underpotential deposition onto defect sites locally accelerates the Au^{3+} reduction kinetics.[60] The protocol, which was originally forwarded and later refined by Vo-Dinh and co-workers,[25,60] is valued because it is free of the cytotoxic shape-directing and capping agents that are commonly used in other nanostar syntheses.[25,26] With a surfactant-free surface, the nanostars can also have superior photocatalytic properties[2,34] and greater near-field enhancements.[35] The synthesis has been carried out using both seedless[9,61,62] and seed-mediated[23,25,60,63] routes where the nanostructure architecture is exquisitely tailored through the variation of (i) reagent concentrations,[25,60–62] (ii) the order and rate at which reagents are added,[25] (iii) pH,[25] (iv) the addition of halides,[60] and (v) seed size.[60] As such, it has become one of the most favored protocols for the synthesis of Au nanostars.

Although AA-driven nanostar syntheses have proven facile, their adaptation to the use of substrate-truncated seeds proved exceedingly difficult. The parameter space, which has proven so amenable to the tailoring of colloidal nanostar properties, consistently yielded little to no growth when applied to the substrate-based seeds. Variations to the Ag^+ concentration, for example, proved to be a powerful tool for varying the architecture of the nanostar colloid (Fig. 4a) but, in all cases, resulted in essentially no growth on the seed array. Colloidal structures, when examined using high-resolution TEM (HRTEM) (Fig. 4b), showed limbs with twin defects running down their length and allowed for a tunable LSPR (Fig. 4c), both of which have been previously observed.[4,60] The divergent nature of the substrate-based results was unexpected because the AA-driven nanostar growth mode is known to rely on defects, yet substrate-based seeds that express the same twin defects[42] as those occurring in the colloidal nanostar limbs were unable to trigger Au^{3+} nucleation.

With syntheses exhibiting near-instantaneous colloidal growth as AA is added and the substrate-based seeds showing

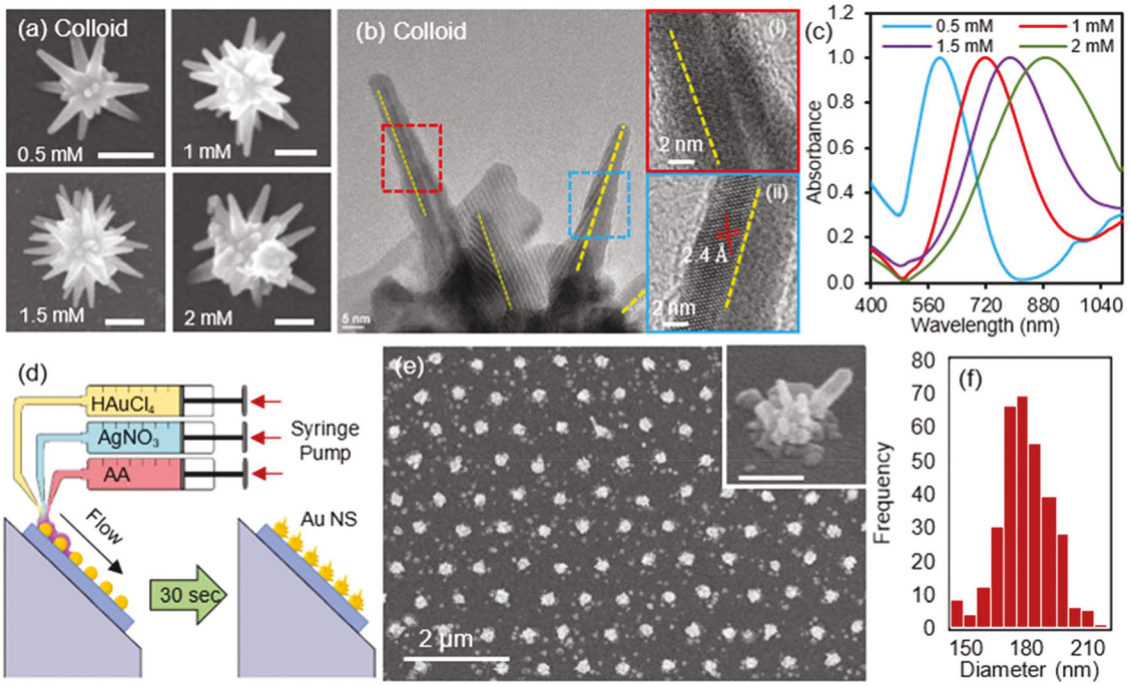

Fig. 4 (a) SEM images of colloidal Au nanostars derived from the AA-driven growth mode for the $AgNO_3$ concentrations labeled on each image (inset scale bar is 200 nm). (b) HRTEM image taken of a single colloidal nanostar with twin boundaries running down the length of each limb (dashed yellow lines). (c) Absorbance spectra for colloidal nanostars derived from syntheses with various $AgNO_3$ concentrations. (d) Schematic of the experimental setup used to flow reactants over substrate-based seeds. (e) SEM image and (f) the corresponding histogram of nanostar diameters.

essentially no growth, it was hypothesized that the arrayed seeds were unable to grow due to (i) the rapid consumption of Au^{3+} by the colloid and (ii) the relative difficulty in sourcing reactants to substrate-immobilized seeds since they 'sample' less reactants even under stirring because of the diminished flow that occurs near surfaces due to the no-slip condition.[64] In an effort to alleviate this disadvantage, the AA-driven growth mode was modified such that each of the three reagents were loaded into syringes and then, using a syringe pump, flowed over a surface as schematically shown in Fig. 4d. The procedure led to the rapid nucleation of Au onto the seeds as well as the self-nucleation of smaller structures directly onto the substrate surface that proved resistant to sonication. Fig. 4e and f shows an SEM image of the so-formed structures and a size distribution histogram of the structures arising from the seed-mediated growth. Variations to the Ag^+ concentration, while resulting in significant changes to nanostructure morphology, did not result in the emergence of well-defined limbs (see ESI, Fig. S7†). Even though the AA-driven growth mode is only able to realize ill-defined structures of poor quality, the transformation from near-zero growth under stirring to rapid uncontrolled growth under a reactant flow is quite remarkable.

2.3. Simulations of the plasmonic properties

The optical response of substrate-supported plasmonic nanostructures is fundamentally different from their colloidal counterparts in that they are subjected to the asymmetric dielectric environment imposed by the substrate.[65,66] Such environments are well-known to red shift the plasmon resonance[67] and enhance the near-fields at the perimeter of the nanostructure where it meets the substrate surface.[68] The structures synthesized in this study not only share these characteristics but further distinguish themselves in that an added asymmetry arises from an apparent truncation by the substrate that leaves the bottom surface of the structure (*i.e.*, the one in contact with the substrate) with a near-atomically-flat planar geometry. With such structures having a fundamentally different character from those previously studied, discrete dipole approximation (DDA) simulations were carried out to isolate these various aspects so as to delineate their influence on the overall optical response.

Although it is recognized that nanostar architectures vary widely, all simulations were based on a relatively simple nanostar geometry comprised of a 110 nm central spherical core from which 18 identical limbs emerge. Such a structure allows for an overall understanding without having the results become unnecessarily obfuscated by the nuances of more erratic geometries. The limbs of the structures used are 27 nm in length, tapered at an angle of 24°, and have tips with a radius of curvature of 3 nm. In free space, these structures exhibit a broad asymmetric plasmon resonance at 644 nm, a value that is red shifted by 119 nm when compared to the response of just the spherical core (see ESI, Fig. S8†). With nanostars typically exhibiting two plasmon modes, where one is associated with the core and the other with the limbs,[3] the

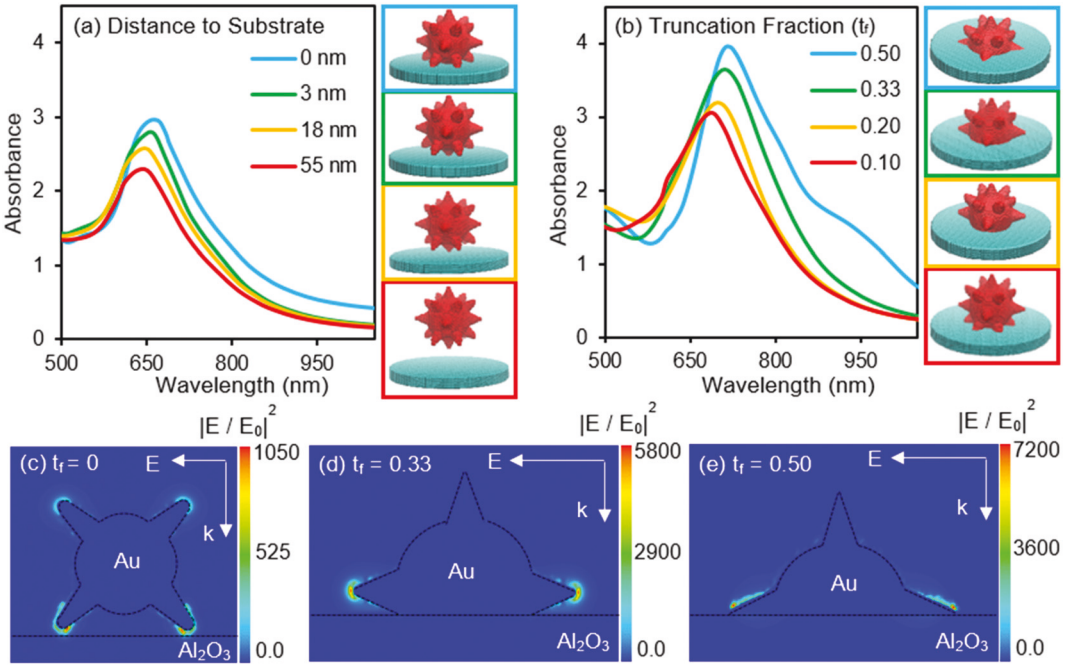

Fig. 5 Simulated absorbance spectra for Au nanostars with a 110 nm core diameter as a function of (a) distance from a sapphire substrate (0–55 nm) and (b) truncation fraction (t_f = 0.1 to 0.5), where curves are color-coded to their respective 3-dimensional models. Incident field and polarization were directed perpendicular and parallel to the substrate, respectively. Calculated near-field enhancement color maps for nanostars that are (c) in contact with the substrate (*i.e.*, t_f = 0) and with truncation fractions of (d) t_f = 0.33 and (e) t_f = 0.50.

observed asymmetry largely arises from an overlap that is exaggerated by the fact that the core diameter is not that different from the limb tip-to-tip distance. The influence of the substrate on the LSPR is made most apparent through simulations showing the progression in the plasmonic response as a nanostar approaches the substrate surface (Fig. 5a). For distances greater than 55 nm, the plasmonic response is little effected by the dielectric environment of the substrate. As the gap width is narrowed further, the LSPR broadens, strengthens, and red shifts. At contact (*i.e.*, the result expected for a colloidal nanostar drop-cast onto the substrate) the LSPR has red shifted a total of 18 nm.

The influence of nanostar truncation on its optical response was also isolated using simulations. The starting point for these simulations was the same nanostar geometry but where it was truncated by varying degrees before locating it on the substrate surface. The degree of truncation is characterized by a truncation fraction, t_f, that specifies the apparent truncation of the spherical core by the substrate surface.[65] Simply stated, a value t_f = 0 leaves the nanostar whole, while a value of t_f = 0.5 sees the nanostar truncated along a plane at its midsection (*i.e.*, cut in half). Fig. 5b shows the simulated absorbance spectra as the truncation fraction is systematically varied between 0.1 and 0.5 as well as schematics of the individual structures. Coinciding with an increase in the truncation fraction from 0.1 to 0.5 is a 27 nm red shift, the emergence of a shoulder at 940 nm, and a substantial rise in absorbance. The shoulder observed for t_f = 0.5 structure is attributed to a longer wavelength plasmon mode that arises when the greatest width of the nanostructure (*i.e.*, its center plane) intersects with a substrate offering increased polarizability. Striking is that the overall rise in absorbance occurs despite the fact that the volume of Au in the nanostructure is steadily diminishing. With the absorbance magnitude representing the ratio of the absorbance cross section to the physical cross section of the structure, it is, hence, evident that the truncated structures interact with incident electromagnetic radiation to an extent that is greater than either a standalone nanostar or one that has been merely drop-cast on the substrate surface. Even though the degree of truncation is not readily varied through experiment,[65] these results nevertheless show that its existence has a decisive impact on the optical response.

With nanostar applications often reliant on the substantial near-field enhancements occurring at limb tips, simulations were carried out that provide an understanding of these enhancements as they relate to substrate-truncated nanostars. Fig. 5c–e shows color maps of the near-field enhancements for nanostars with three different truncation fractions. When the nanostar is resting on the substrate surface (t_f = 0), substantial enhancements occur at the limb tips but where the two limbs that are in contact with the substrate show a 4-fold enhancement in the maximum near-field intensity when compared to identical limbs extending out into free-space. This asymmetry in the near-fields is as expected since the dielectric environment provided by the substrate preferentially promotes electron oscillations in metal nanostructure for regions nearer to its surface.[65] When compared to the nanostar resting on the substrate surface, structures with truncation fractions of 0.33

and 0.50 show maximum near-field intensities that are five and seven times greater, respectively. Such enhancements arise from limbs being parallel to both the substrate surface and the electric field vector (**E**) of the incident light with maximum values occurring when the nanostar limbs intersect with the surface (Fig. 5e). These simulations demonstrate that truncated structures can lead to far greater near-fields than structures that are merely resting on the substrate surface such as those obtained through the drop-casting of colloidal structures.

2.4 SERS using periodic arrays of Au nanostar

Au nanostars derived from colloidal syntheses have been demonstrated as highly efficient SERS substrates due to their multi-limbed morphology.[15,17] Prior work has, for the most part, utilized either passive techniques[11,16] (*e.g.*, drop-casting) or surface-functionalization[14,18] to assemble nanostar populations on planar surfaces. Such techniques can, however, lead to an inconsistent surface coverage and result in a substantial SERS background signal. Although the reproducibility can be compromised by these approaches, SERS enhancement factors (EFs) between 10^6 and 10^8 are commonly observed in the detection of a variety of molecular species.[11,44,69] With DDA simulations showing greater absorbance efficiency and superior near-field intensities for the truncated nanostar geometry, studies were carried out that assess the various arrays as SERS substrates. It should be noted that the arrayed nature of these SERS substrates, with a periodicity of 600 nm, precludes the formation of the SERS hot spots that typically form when nanostars agglomerate on surfaces. As such, the EF values obtained more accurately reflect that of a standalone structure. Moreover, accuracy in the EF value is derived from the fact that the number of nanostars within the probe beam is accurately known.

Thiophenol was chosen as a SERS probe molecule for its ability to form self-assembled monolayers on Au surfaces.[70] Nanostar arrays derived from each of the three growth modes were examined where quantitative analysis relied on the EF metric defined by eqn (1).[71]

$$\mathrm{EF} = \frac{\left(\frac{I_{\mathrm{SERS}}}{N_{\mathrm{molecules}}}\right)}{\left(\frac{I_{\mathrm{Raman}}}{N_{\mathrm{Raman}}}\right)} \quad (1)$$

Fig. 6 shows the background subtracted SERS spectra for all three cases as well as the Raman spectra used to calculate the average EF values. It should be noted that measurements performed on just the Au seed array showed no measurable SERS enhancement. The SERS spectra show three prominent peaks corresponding to the (i) ring out-of-plane deformation and C–H out-of-plane bending modes (999 cm^{-1}), (ii) ring in-plane deformation and C–C symmetric stretching modes (1022 cm^{-1}), and (iii) C–C symmetric stretching and C–S stretching modes (1074 cm^{-1}).[72–74] Calculated EF values for the HEPES-, DMF-, and AA-driven growth modes were 7×10^5, 1×10^7, and 2×10^6 respectively (see ESI† for details). Striking

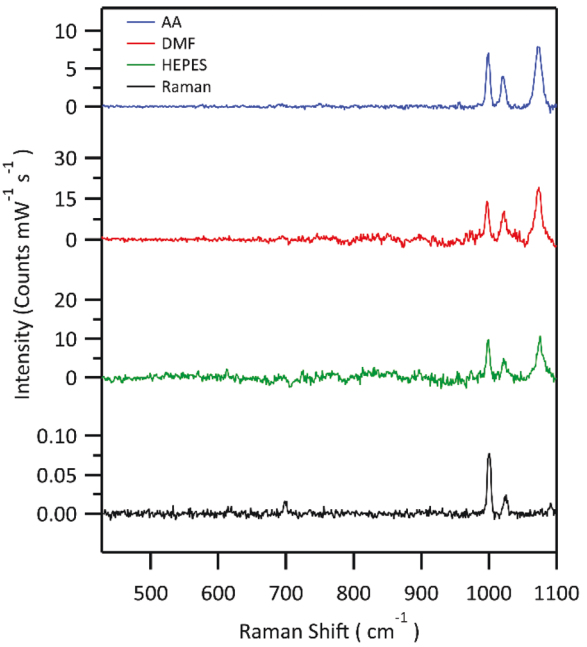

Fig. 6 Representative SERS spectra for thiophenol monolayer detection by periodic arrays of nanostars derived from HEPES-, DMF-, and AA-driven syntheses as well as the Raman spectra used in the EF calculation.

is that these values, despite the absence of hot spots, are comparable to those obtained in many nanostar studies.[75,76]

3. Discussion

Three distinctly different colloidal nanostar syntheses were carried out on substrate-based seeds but only the DMF-driven mode was able to yield a product that was comparable to that of the colloid. This mode is unique in that (i) it is carried out in a non-aqueous environment, (ii) the reaction kinetics are slow, and (iii) there is less competition for reactants from colloidal nanostructures generated from spontaneously formed seeds. In stark contrast, the AA-driven growth mode was unable to even nucleate significant amounts of Au on the substrate-based seeds under conditions that gave rise to impressive colloidal nanostars with long and well-defined limbs. It did, however, lead to rapid growth when the same reactants were flowed over the substrate surface. This finding points toward kinetics as being a decisive factor. It is also interesting that none of the three growth modes seem to be impacted, either positively or negatively, by the fact that the substrate-based seeds are lined with twin defects, even though such defects are commonly observed in nanostars.[4,60] This assessment is based on the fact that these defects consistently align parallel to the substrate surface[42] and that, with the exception of the result shown in Fig. 2b, there is no indication of preferential growth in this direction. Even this exception did not realize a spiked morphology. Spiked growth could therefore require a more complex trigger such as the intersection of multiple twins.

Although the adaptation of these nanostar growth modes to substrate-immobilized seeds proves challenging, intrinsic advantages exist. In their preparation, it is possible to (i) quickly terminate growth by removing the substrate from the reactants, (ii) separate the desired seed-mediated growth from the unwanted spontaneous growth through sonication, and (iii) easily remove unwanted, and often detrimental, capping agents through post-growth cleaning procedures without the possibility of nanostar agglomeration. From a durability standpoint, the substrate-based structures have proven robust to sonication, a quality that lends itself to cleaning and reuse in sensing applications. Moreover, these structures are not subject to the long-term shape-changes when stored in air. In contrast, colloid instability has been a persistent issue in the application of Au nanostars as facile SERS substrate components because the sharp geometry of nanostar limbs soften and eventually disappear altogether under heat or lengthy exposures to aqueous environments.[77,78] Such effects, have also been observed for the colloids produced in this study on time scales as short as 24 h (see ESI, Fig. S9†). Additionally, the use of near-hemispherical seeds in the DMF-driven growth mode, not only gives rise to monodisperse nanostars in high yield, but also results in a nanostar morphology that is distinct from its colloidal counterpart due to an apparent truncation by the substrate. This difference is not merely aesthetic but can result in significantly higher near-fields than conventional nanostars dispersed on the same substrate surface. With these substrate-based nanostars being amenable to both size uniformity and precise placement, also comes the possibility of dramatically amplifying SERS signals through the placement of nanostars in close enough proximity to realize a high density of hot-spots near the substrate surface.

4. Conclusion

In this study, we have applied three different seed-mediated Au nanostar syntheses to periodic arrays of near-hemispherical substrate-immobilized Au seeds fabricated using nanoimprint lithography in combination with templated-dewetting. The DMF-driven synthesis proved the most successful, yielding nanostars with numerous short sharp spikes at a near-one-hundred percent yield. The structures showed SERS enhancement factors as high as 10^7 for the thiophenol probe molecule, a result that was attributed to the exaggerated near-fields that are present when nanostar spikes are adjacent to the substrate surface. These findings advance the use of nanostars for wafer-based applications and provide the impetus for further studies directed toward establishing synthetic controls for substrate-based nanostars that rival those of their colloidal counterparts.

5. Experimental section

5.1. Materials

Au and Sb film depositions were carried out using targets cut from a 0.5 mm thick foil with 99.9985% purity (Alfa Aesar) and a 19 mm diameter rod (ESPI metals) with 99.999% purity, respectively. Two-side polished [0001]-oriented sapphire substrates with dimensions of 10 mm × 10.5 mm × 0.65 mm were cut from 100 mm diameter wafers (MTI Corporation). The nanoimprint lithographic process utilized a (i) moldable polymer resist (mr-I 7030R, Micro Resist Technology, GmbH), (ii) silicon stamp (Lightsmyth Technologies), and (iii) trichloro (1*H*,1*H*,2*H*,2*H*-perfluoro-octyl)silane antisticking layer (Sigma Aldrich). Ultrahigh purity Ar was used as the processing gas in the Au seed assembly process. The reagents used in the various nanostar syntheses are hydrogen tetrachloroaurate(III) trihydrate (99.99% Alfa Aesar), hydrochloric acid (VWR), sodium hydroxide (VWR), silver nitrate (>99.9% Alfa Aesar), 4-(2-hydroxyethyl)-1-piperazineethanesulfonic acid (HEPES buffer) (99% VWR), *N*,*N*-dimethylformamide (DMF) (Beantown Chemical), polyvinylpyrolidone mol wt 40 000 (PVP) (99% Sigma Aldrich), and ascorbic acid (>99% Sigma Aldrich). SERS analysis was carried out using benzene thiol (≥99%, Sigma Aldrich). All aqueous solutions were prepared using deionized water (DI) water from a Milli-Q system (18.2 MΩ cm at 25 °C).

5.2. Au seed arrays

Periodic arrays of Au seeds were prepared using a templated assembly route that is described in detail elsewhere.[42,43] Briefly, a moldable resist is spin-coated over the substrate surface after which a nanoimprint lithography process is used to define a hexagonal array of cylindrical openings (diameter = 240 nm, length = 350 nm, center-to-center distance = 600 nm) through which Sb (t = 12 nm) and Au (t = 2.5 nm) layers are sequentially sputter deposited. A lift-off procedure is then used to remove the remaining resist as well as excess Au and Sb to reveal an array of disc-shaped Au–Sb pedestals. The pedestals are then exposed to a heating regimen (ramped to 1010 °C in flowing Ar) in which the sublimation of the sacrificial Sb layer causes the Au overlayer to assemble into a highly crystalline seed.[79]

5.3. HEPES-driven nanostar synthesis

The synthetic procedure for Au nanostar formation was adapted from the protocol set forth by Xie *et al.*[36] An aqueous room temperature HEPES buffer solution (8.4 ml, 250 mM) was added to a 30 ml Pyrex beaker after which the pH of the solution was set to the desired value through the addition of NaOH (200 μl, 30–100 mM). The substrate-supported Au seed array was then inserted into the solution such that it rests face-up at the bottom of the beaker toward one edge so as not to interfere with magnetic stirring (350 rpm). Aqueous $HAuCl_4$ (1 ml, 10 mM) was then quickly added, followed by a 30 s dropwise addition of aqueous $AgNO_3$ (400 μl, 2–5 mM). The stirring rate was then increased to 700 rpm for the remainder of the 15 min synthesis that sees the solution slowly transform from a faint yellow to a dark blue color. Upon completion, the substrate was retrieved from the solution, rinsed with DI water, and sonicated for 30 s in isopropanol to remove any colloidally-formed nanostructures from its surface. The remaining

colloid was centrifuged three times for 45 min at 4400 rpm where redispersal occurred in a 50%/50% acetone/DI water mixture. The remaining colloid was drop-cast on glass for imaging.

5.4. DMF-driven nanostar synthesis

The DMF-based protocol used for Au nanostar synthesis was adapted from the synthetic procedure forwarded by Kumar *et al.*[19] This room temperature synthesis, which was also carried out in a 30 ml Pyrex beaker, sees 1.8 g of PVP dissolved in 10 ml of DMF and stirred at 700 rpm. The substrate-supported seed array was then inserted into the beaker, followed by the rapid addition of aqueous $HAuCl_4$ (300 μl, 10 mM). After a 60 min interval, the substrate was retrieved from the beaker and rinsed using the aforementioned procedures. The colloid was centrifuged at 4400 rpm for 45 min, redispersed in DI water, and drop-cast.

5.5. AA-driven nanostar synthesis

Au nanostar fabrication was implemented as a variation on the synthetic protocol described by Yuan *et al.*[25] Initial syntheses yielding only colloidal nanostars were carried out in a 30 ml glass beaker and proceeded through the addition of 10 ml of 0.75 mM $HAuCl_4$ followed by the adjustment of the solution pH to the desired value through the addition of NaOH or HCl. Stirring at 700 rpm was then initiated, followed by the simultaneous addition of 400 μl of $AgNO_3$ (0.5–2 mM) and 200 μl of 100 mM AA. Upon addition, the solution turned from clear to pink and then to dark blue in a few seconds. Nanostars were washed once in isopropanol before drop-casting. Syntheses yielding substrate-based structures flowed reactants over Au seeds supported on a substrate that was tilted at a 60° angle from the horizontal. Three reactants, $HAuCl_4$, (1 mM), AA (100 mM), and $AgNO_3$ (0.5–2 mM), were simultaneously flowed onto the substrate for 30 s at 9 ml min^{-1} using three separate syringes that were pointed to approximately the same location and driven by a syringe pump. The mixture was a light purple during the brief interval in which it was in contact with the seed array but then rapidly turned a deep bluish purple once it flowed off the substrate and collected in a beaker. The substrate was subsequently removed, sonicated in DI water, rinsed with isopropanol, and dried.

5.6. Simulation details

DDA simulations were carried out using the DDSCAT 7.3 software package.[80] Nanocrystal geometry is represented by a finite three-dimensional cubic array of individually polarizable points where each is assigned the dielectric properties of bulk Au. When subjected to an oscillating external electric field (*i.e.*, light), each of the points acquires a dipole moment from which the scattering and absorption cross sections of the nanocrystal are calculated. Nanocrystal geometries are designed using the LAMMPS[81] software package and visualized using Visual Molecular Dynamics (VMD).[82] For all simulations, the total number of dipoles defining the Au nanostar morphologies and substrate was approximately 100 000, a value that was held constant to within 0.1% between various models. The dielectric constants for Au and sapphire were taken from well-accepted sources.[83,84]

5.7. Surface enhanced Raman spectroscopy

Surface-enhanced Raman spectroscopy (SERS) was carried out using a home-built set-up. A 633 nm HeNe laser (Thorlabs) was directed into an inverted microscope (Nikon Ti-U) and focused onto the substrate with an objective lens (20×, NA = 0.5). Scattered light was collected through the same objective, filtered through a Rayleigh rejection filter (Semrock), and fed into a spectrometer (Princeton Instruments Action SP2300, f = 0.3 mm, 1200 g mm^{-1}). Spectra were analyzed using Winspec32 software (Princeton Instruments). Samples for SERS characterization were prepared *via* gas phase adsorption, where substrates were placed in a sealed petri dish with a vial containing 10 μL of neat benzene thiol (*i.e.*, thiophenol) for 21 h. The substrate was then removed and SERS spectra were acquired. After SERS acquisition, the sample was washed in methanol for reuse. Triplicate Raman and SERS spectra were averaged and processed using Igor Multipeak Fitting 2.0 software for peak area analysis. The background spectra showed two strong peaks at 420 cm^{-1} and 750 cm^{-1} (see ESI, Fig. S10†). EF values were calculated using the three prominent modes at 999, 1022, and 1074 cm^{-1}. The laser spot size diameter (d) was approximated as 1.54 μm using the diameter of an Airy disk and assuming a perfect focus for a Gaussian beam.[85] The scattering volume (V) was approximated as 7.5×10^{-12} mL assuming a laser beam that is modeled as a cylinder[86] with height equal to the depth of field.[85] The thiophenol molecule surface coverage was calculated by approximating each nanostar as a hemisphere with conical limbs and that a self-assembled monolayer formed with a surface density of 6.8×10^{14} molecules per cm^2.[70] The sum of the three Raman mode peak areas were normalized to the number of thiophenol molecules within the Rayleigh range for both the Raman scattering and SERS substrates.

5.8. Instrumentation

Sputter depositions were carried out in a Model 681 Gatan High Resolution Ion Beam Coater. Nanoimprint lithography utilized a Laurell Spin Coater, SAMCO RIE-1C Reactive Ion Etcher, and a home-built press.[43] SEM images were obtained using a Helios G4 Ux SEM/FIB Workstation (FEI). TEM imaging was carried out using an FEI Titan 80-300 Transmission Electron Microscope. LSPR spectra were recorded using a JASCO V-730 UV–Visible Spectrophotometer. All pH measurements were carried out using a HM Digital PH-200 pH meter.

Conflicts of interest

There are no conflicts to declare.

Acknowledgements

This work is supported by National Science Foundation Awards DMR-1803917 to S. N. and CHE-1709881 to J. P. C. It has also benefited from the facilities available through the Notre Dame Integrated Imaging Facility (NDIIF). T. B. D. wishes to acknowledge M. Stroik and M. Glazman (Trinity School at Greenlawn) for assistance with laboratory work.

Notes and references

1 J. Wua, P. Yu, A. S. Susha, K. A. Sablon, H. Chen, Z. Zhou, H. Li, H. Ji, X. Niu, A. O. Govorov, A. L. Rogach and Z. M. Wang, *Nano Energy*, 2015, **13**, 827–835.
2 S. Atta, A. M. Pennington, F. E. Celik and L. Fabris, *Chem*, 2018, **4**, 2140–2153.
3 A. Guerrero-Martinez, S. Barbosa, I. Pastoriza-Santos and L. M. Liz-Marzán, *Curr. Opin. Colloid Interface Sci.*, 2011, **16**, 118–127.
4 S. Atta, M. Beetz and L. Fabris, *Nanoscale*, 2019, **11**, 2946–2958.
5 D. Huo, Z. Cao, J. Li, M. Xie, J. Tao and Y. Xia, *Nano Lett.*, 2019, **19**, 3115–3121.
6 J. D. Smith, Z. J. Woessner and S. E. Skrabalak, *J. Phys. Chem. C*, 2019, **123**, 18113–18123.
7 W. Niu, Y. A. A. Chua, W. Zhang, H. Huang and X. Lu, *J. Am. Chem. Soc.*, 2015, **137**, 10460–10463.
8 S. Atta, T. V. Tsoulos and L. Fabris, *J. Phys. Chem. C*, 2016, **120**, 20749–20758.
9 S. Umadevi, H. C. Lee, V. Ganesh, X. Feng and T. Hegmann, *Liq. Cryst.*, 2014, **41**, 265–276.
10 A. Kedia and P. S. Kumar, *J. Phys. Chem. C*, 2012, **116**, 23721–23728.
11 S. K. Krishnan and Y. C. Godoy, *ACS Omega*, 2020, **5**, 1384–1393.
12 D. M. Solís, J. M. Taboada, F. Obelleiro, L. M. Liz-Marzán and F. J. García De Abajo, *ACS Photonics*, 2017, **4**, 329–337.
13 S. Harmsen, R. Huang, M. A. Wall, H. Karabeber, J. M. Samii, M. Spaliviero, J. R. White, S. Monette, R. O'Connor, K. L. Pitter, S. A. Sastra, M. Saborowski, E. C. Holland, S. Singer, K. P. Olive, S. W. Lowe, R. G. Blasberg and M. F. Kircher, *Sci. Transl. Med.*, 2015, **7**, 271ra7.
14 O. Bibikova, J. Haas, A. I. López-Lorente, A. Popov, M. Kinnunen, I. Meglinski and B. Mizaikoff, *Analyst*, 2017, **142**, 951–958.
15 S. Park, J. Lee and H. Ko, *ACS Appl. Mater. Interfaces*, 2017, **9**, 44088–44095.
16 A. S. D. S. Indrasekara, S. Meyers, S. Shubeita, L. C. Feldman, T. Gustafsson and L. Fabris, *Nanoscale*, 2014, **6**, 8891–8899.
17 J. Cyriac, G. Li and R. G. Cooks, *Anal. Chem.*, 2011, **83**, 5114–5121.
18 Q. Su, X. Ma, J. Dong, C. Jiang and W. Qian, *ACS Appl. Mater. Interfaces*, 2011, **3**, 1873–1879.
19 P. S. Kumar, I. Pastoriza-Santos, B. Rodrigues-Gonzalez and F. J. Garcia de Abajo, *Nanotechnology*, 2008, **19**, 015606.
20 C. G. Khoury and T. Vo-Dinh, *J. Phys. Chem. C*, 2008, **112**(48), 8849–18859.
21 R. M. Pallares, T. Stilson, P. Choo, J. Hu and T. W. Odom, *ACS Appl. Nano Mater.*, 2019, **2**, 5266–5271.
22 K. Nehra, S. K. Pandian, M. S. S. Bharati and V. R. Soma, *New J. Chem.*, 2019, **43**, 3835–3847.
23 I. G. Theodorou, P. Ruenraroengsak, D. A. Gonzalez-Carter, Q. Jiang, E. Yagüe, E. O. Aboagye, R. C. Coombes, A. E. Porter, M. P. Ryan and F. Xie, *Nanoscale*, 2019, **11**, 2079–2088.
24 M. Amjadi and Z. Abolghasemi, *Sens. Actuators, B*, 2018, **257**, 629–634.
25 H. Yuan, C. G. Khoury, H. Hwang, C. M. Wilson, G. A. Grant and T. Vo-Dinh, *Nanotechnology*, 2012, **23**, 075102.
26 D. Li, Y. Zhang, S. Wen, Y. Song, Y. Tang, X. Zhu, M. Shen, S. Mignani, J. P. Majoral, Q. Zhao and X. Shi, *J. Mater. Chem. B*, 2016, **4**, 4216–4226.
27 Y. Wang, K. C. L. Black, H. Luehmann, W. Li, Y. Zhang, X. Cai, D. Wan, S. Y. Liu, M. Li and P. Kim, *ACS Nano*, 2013, **7**, 2068–2077.
28 H. Yuan, C. G. Khoury, C. M. Wilson, G. A. Grant, A. J. Bennett and T. Vo-Dinh, *Nanomedicine*, 2012, **8**, 1355–1363.
29 H. Yuan, A. M. Fales and T. Vo-Dinh, *J. Am. Chem. Soc.*, 2012, **134**, 11358–11361.
30 S. Z. Nergiz, N. Gandra, S. Tadepalli and S. Singamaneni, *ACS Appl. Mater. Interfaces*, 2014, **6**, 16395–16402.
31 D. H. M. Dam, J. H. Lee, P. N. Sisco, D. T. Co, M. Zhang, M. R. Wasielewski and T. W. Odom, *ACS Nano*, 2012, **6**, 3318–3326.
32 Y. Liu, P. Maccarini, G. M. Palmer, W. Etienne, Y. Zhao, C. Lee, X. Ma, B. A. Inman and T. Vo-Dinh, *Sci. Rep.*, 2017, **7**, 8606.
33 J. Liu, H. Cui, S. Yan, X. Jing, D. Wang and L. Meng, *Mater. Today Commun.*, 2018, **16**, 97–104.
34 L. Wang, Y. Wang, P. Schmuki, S. Kment and R. Zboril, *Electrochim. Acta*, 2018, **260**, 212–220.
35 W. Kim, N. Kim, J. W. Park and Z. H. Kim, *Nanoscale*, 2016, **8**, 987–994.
36 J. Xie, J. Y. Lee and D. I. C. Wang, Seedless, *Chem. Mater.*, 2007, **19**, 2823–2830.
37 W. A. El-Said, S. U. Kim and J. W. Choi, *J. Mater. Chem. C*, 2015, **3**, 3848–3859.
38 Y. Zhaoa, X. Li, Y. Liu, L. Zhang, F. Wang and Y. Lu, *Sens. Actuators, B*, 2017, **247**, 850–857.
39 L. Osinkina, T. Lohmüller, F. Jäckel and J. Feldmann, *J. Phys. Chem. C*, 2013, **117**, 22198–22202.
40 R. A. Hughes, E. Menumerov and S. Neretina, *Nanotechnology*, 2017, **28**, 282002.
41 S. Neretina, R. A. Hughes, K. D. Gilroy and M. Hajfathalian, *Acc. Chem. Res.*, 2016, **49**, 2243–2250.
42 S. D. Golze, R. A. Hughes, S. Rouvimov, R. D. Neal, T. B. Demille and S. Neretina, *Nano Lett.*, 2019, **19**, 5653–5660.

43 E. Menumerov, S. D. Golze, R. A. Hughes and S. Neretina, *Nanoscale*, 2018, **10**, 18186–18194.
44 H. I. Khan, M. U. Khalid, A. Abdullah, A. Ali, A. S. Bhatti, S. U. Khan and W. Ahmed, *J. Vac. Sci. Technol., B: Nanotechnol. Microelectron.: Mater., Process., Meas., Phenom.*, 2017, **36**, 03E101.
45 K. Chandra, K. S. B. Culver, S. E. Werner, R. C. Lee and T. W. Odom, *Chem. Mater.*, 2016, **28**, 6763–6769.
46 H. De Puig, J. O. Tam, C. W. Yen, L. Gehrke and K. Hamad-Schifferli, *J. Phys. Chem. C*, 2015, **119**, 17408–17415.
47 Q. Xi and A. J. Haes, *J. Am. Chem. Soc.*, 2019, **141**, 4034–4042.
48 K. Chandra, V. Kumar, S. E. Werner and T. W. Odom, *ACS Omega*, 2017, **2**, 4878–4884.
49 D. W. Mulder, M. M. Phiri, A. Jordaan and B. C. Vorster, *R. Soc. Open Sci.*, 2019, **6**, 190160.
50 A. Habib, M. Tabata and Y. G. Wu, *Bull. Chem. Soc. Jpn.*, 2005, **78**, 262–269.
51 I. Pastoriza-Santos and L. M. Liz-Marzan, *Adv. Funct. Mater.*, 2009, **19**, 679–688.
52 T. S. Rodrigues, M. Zhao, T. H. Yang, K. D. Gilroy, A. G. M. da Silva, P. H. C. Camargo and Y. Xia, *Chem. – Eur. J.*, 2018, **24**, 16944–16963.
53 K. M. Koczkur, S. Mourdikoudis, L. Polavarapu and S. E. Skrabalak, *Dalton Trans.*, 2015, **44**, 17883–17905.
54 Y. Gao, P. Jiang, L. Song, J. X. Wang, L. F. Liu, D. F. Liu, Y. J. Xiang, Z. X. Zhang, X. W. Zhao, X. Y. Dou, S. D. Luo, W. Y. Zhou and S. S. Xie, *J. Cryst. Growth*, 2006, **289**, 376–380.
55 A. Sanchez-Iglesias, I. Pastoriza-Santos, J. Perez-Juste, B. Rodrıguez-Gonzalez, F. J. Garcıa de Abajo and L. M. Liz-Marzan, *Adv. Mater.*, 2006, **18**, 2529–2534.
56 M. Tsuji, R. Matsuo, P. Jiang, N. Miyamae, D. Ueyama, M. Nishio, S. Hikino, H. Kumagae, K. S. N. Kamarudin and X. L. Tang, *Cryst. Growth Des.*, 2008, **8**, 2528–2536.
57 A. Kedia and P. S. Kumar, *J. Mater. Chem. C*, 2013, **1**, 4540–4549.
58 A. Kedia and P. S. Kumar, *J. Phys. Chem. C*, 2012, **116**, 1679–1686.
59 P. Abella, B. Garcia-Cueto, F. Gonzalez, F. Moreno, P. C. Wu, T. H. Kim, A. Brown, Y. Yang, H. O. Everitt and G. Videen, *Nano Lett.*, 2011, **11**, 3531–3537.
60 A. S. D. S. Indrasekara, S. F. Johnson, R. A. Odion and T. Vo-Dinh, *ACS Omega*, 2018, **3**, 2202–2210.
61 L. C. Cheng, J. H. Huang, H. M. Chen, T. C. Lai, K. Y. Yang, R. S. Liu, M. Hsiao, C. H. Chen, L. J. Her and D. P. Tsai, *J. Mater. Chem.*, 2012, **22**, 2244–2253.
62 S. He, M. W. C. Kang, F. J. Khan, E. M. K. Tan, M. A. Reyes and J. C. Y. Kah, *J. Opt.*, 2015, **17**, 114013.
63 Y. Li, J. Ma and Z. Ma, *Electrochim. Acta*, 2013, **108**, 435–440.
64 P. A. Thompson and S. M. Troian, *Nature*, 1997, **389**, 360–362.
65 T. B. Demille, R. A. Hughes and S. Neretina, *J. Phys. Chem. C*, 2019, **123**, 19879–19886.
66 B. J. Wiley, S. H. Im, Z. Y. Li, J. McLellan, A. Siekkinen and Y. Xia, *J. Phys. Chem. B*, 2006, **110**, 15666–15675.
67 M. D. Malinsky, K. L. Kelly, G. C. Schatz and R. P. Van Duyne, *J. Phys. Chem. B*, 2001, **105**, 2343–2350.
68 J. Quan, J. Zhang, X. Qi, J. Li, N. Wang and Y. Zhu, *Sci. Rep.*, 2017, **7**, 14771.
69 W. Zhang, N. Large and H. Wang, *ACS Appl. Mater. Interfaces*, 2014, **6**, 17255–17267.
70 C. M. Whelan, M. R. Smyth and C. J. Barnes, *Langmuir*, 1999, **15**, 116–126.
71 E. C. Le Ru, E. Blackie, M. Meyer and P. G. Etchegoint, *J. Phys. Chem. C*, 2007, **111**, 13794–13803.
72 S. Li, D. Wu, X. Xu and R. Gu, *J. Raman Spectrosc.*, 2007, **38**, 1436–1443.
73 K. T. Carron and L. G. Hurley, *J. Phys. Chem.*, 1991, **95**, 9979–9984.
74 K. B. Biggs, J. P. Camden, J. N. Anker and R. P. Van Duyne, *J. Phys. Chem. A*, 2009, **113**, 4581–4586.
75 H. M. Jin, J. Y. Kim, M. Heo, S.-J. Jeong, B. H. Kim, S. K. Cha, K. H. Han, J. H. Kim, G. G. Yang, J. Shin and S. O. Kim, *ACS Appl. Mater. Interfaces*, 2018, **10**, 44660–44667.
76 J. F. Bryche, R. Gillibert, G. Barbillon, P. Gogol, J. Moreau, M. Lamy de la Chapelle, B. Bartenlian and M. Canva, *Plasmonics*, 2016, **11**, 601–608.
77 M. M. Vega, A. Bonifacio, V. Lughi, S. Marsi, S. Carrato and V. Sergo, *J. Nanopart. Res.*, 2014, **16**, 2729.
78 W. Xi, H. T. Phan and A. J. Haes, *Anal. Bioanal. Chem.*, 2018, **410**, 6113–6123.
79 P. Farzinpour, A. Sundar, K. D. Gilroy, Z. E. Eskin, R. A. Hughes and S. Neretina, *Nanoscale*, 2013, **5**, 1929–1938.
80 B. T. Draine and P. J. Flatau, User Guide to the Discrete Dipole Approximation Code DDSCAT (7.3) 2013, arXiv:1305.6497v1, arXiv.org e-Print archive.
81 S. J. Plimpton, *Comput. Phys.*, 1995, **117**, 1.
82 W. Humphrey, A. Dalke and K. Schulten, *J. Mol. Graphics*, 1996, **14**, 33–38.
83 P. B. Johnson and R. W. Christy, *Phys. Rev. B: Solid State*, 1972, **6**, 4370–4379.
84 E. D. Palik, *Handbook of Optical Constant of Solids*, Academic Press, New York, NY, 1998.
85 R. A. Álvarez-Puebla, *J. Phys. Chem. Lett.*, 2012, **3**, 857–866.
86 A. D. McFarland, M. A. Young, J. A. Dieringer and R. P. Van Duyne, *J. Phys. Chem. B*, 2005, **109**, 11279–11285.